A dual-modal retinal imaging system with adaptive optics

Alexander Meadway,[1*] Christopher A. Girkin,[1] and Yuhua Zhang[1,2,3]

[1]*Department of Ophthalmology, University of Alabama at Birmingham, 1670 University Boulevard, Birmingham, AL 35294, USA*
[2]*Department of Vision Sciences, University of Alabama at Birmingham, 1530 3rd Avenue South, Birmingham, AL 35294, USA*
[3]*Department of Biomedical Engineering, University of Alabama at Birmingham, 1825 University Boulevard, Birmingham, AL 35294, USA*
**meadway@uab.edu*

Abstract: An adaptive optics scanning laser ophthalmoscope (AO-SLO) is adapted to provide optical coherence tomography (OCT) imaging. The AO-SLO function is unchanged. The system uses the same light source, scanning optics, and adaptive optics in both imaging modes. The result is a dual-modal system that can acquire retinal images in both *en face* and cross-section planes at the single cell level. A new spectral shaping method is developed to reduce the large sidelobes in the coherence profile of the OCT imaging when a non-ideal source is used with a minimal introduction of noise. The technique uses a combination of two existing digital techniques. The thickness and position of the traditionally named inner segment/outer segment junction are measured from individual photoreceptors. *In-vivo* images of healthy and diseased human retinas are demonstrated.

OCIS codes: (110.4500) Optical coherence tomography; (110.1080) Active or adaptive optics; (170.4460) Ophthalmology; (170.4470) Scanning laser ophthalmoscope.

References and links

1. R. H. Webb, G. W. Hughes, and O. Pomerantzeff, "Flying spot TV ophthalmoscope," Appl. Opt. **19**(17), 2991–2997 (1980).
2. R. H. Webb, G. W. Hughes, and F. C. Delori, "Confocal scanning laser ophthalmoscope," Appl. Opt. **26**(8), 1492–1499 (1987).
3. D. Huang, E. A. Swanson, C. P. Lin, J. S. Schuman, W. G. Stinson, W. Chang, M. R. Hee, T. Flotte, K. Gregory, C. A. Puliafito, and et, "Optical coherence tomography," Science **254**(5035), 1178–1181 (1991).
4. T. Wilson, *Confocal Microscopy* (Academic Press, 1990).
5. A. Roorda, "Applications of adaptive optics scanning laser ophthalmoscopy," Optom. Vis. Sci. **87**(4), 260–268 (2010).
6. R. Yadav, K. S. Lee, J. P. Rolland, J. M. Zavislan, J. V. Aquavella, and G. Yoon, "Micrometer axial resolution OCT for corneal imaging," Biomed. Opt. Express **2**(11), 3037–3046 (2011).
7. W. Drexler, U. Morgner, F. X. Kärtner, C. Pitris, S. A. Boppart, X. D. Li, E. P. Ippen, and J. G. Fujimoto, "In vivo ultrahigh-resolution optical coherence tomography," Opt. Lett. **24**(17), 1221–1223 (1999).
8. A. Roorda, F. Romero-Borja, W. Donnelly Iii, H. Queener, T. Hebert, and M. Campbell, "Adaptive optics scanning laser ophthalmoscopy," Opt. Express **10**(9), 405–412 (2002).
9. B. Hermann, E. J. Fernández, A. Unterhuber, H. Sattmann, A. F. Fercher, W. Drexler, P. M. Prieto, and P. Artal, "Adaptive-optics ultrahigh-resolution optical coherence tomography," Opt. Lett. **29**(18), 2142–2144 (2004).
10. W. H. Woon, F. W. Fitzke, A. C. Bird, and J. Marshall, "Confocal imaging of the fundus using a scanning laser ophthalmoscope," Br. J. Ophthalmol. **76**(8), 470–474 (1992).
11. J. Liang, D. R. Williams, and D. T. Miller, "Supernormal vision and high-resolution retinal imaging through adaptive optics," J. Opt. Soc. Am. A **14**(11), 2884–2892 (1997).
12. Y. Zhang, S. Poonja, and A. Roorda, "MEMS-based adaptive optics scanning laser ophthalmoscopy," Opt. Lett. **31**(9), 1268–1270 (2006).
13. Y. Zhang, S. Poonja, and A. Roorda, *AOSLO: from Benchtop to Clinic*, M. K. Giles, J. D. Gonglewski, and R. A. Carreras, eds. (2006), Vol. 6306, pp. 63060V1–63060V–11.

#198069 - $15.00 USD Received 23 Sep 2013; revised 1 Nov 2013; accepted 12 Nov 2013; published 25 Nov 2013

14. S. A. Burns, R. Tumbar, A. E. Elsner, D. Ferguson, and D. X. Hammer, "Large-field-of-view, modular, stabilized, adaptive-optics-based scanning laser ophthalmoscope," J. Opt. Soc. Am. A **24**(5), 1313–1326 (2007).
15. D. C. Chen, S. M. Jones, D. A. Silva, and S. S. Olivier, "High-resolution adaptive optics scanning laser ophthalmoscope with dual deformable mirrors," J. Opt. Soc. Am. A **24**(5), 1305–1312 (2007).
16. D. C. Gray, W. Merigan, J. I. Wolfing, B. P. Gee, J. Porter, A. Dubra, T. H. Twietmeyer, K. Ahamd, R. Tumbar, F. Reinholz, and D. R. Williams, "In vivo fluorescence imaging of primate retinal ganglion cells and retinal pigment epithelial cells," Opt. Express **14**(16), 7144–7158 (2006).
17. N. M. Putnam, D. X. Hammer, Y. Zhang, D. Merino, and A. Roorda, "Modeling the foveal cone mosaic imaged with adaptive optics scanning laser ophthalmoscopy," Opt. Express **18**(24), 24902–24916 (2010).
18. A. Dubra and Y. Sulai, "Reflective afocal broadband adaptive optics scanning ophthalmoscope," Biomed. Opt. Express **2**(6), 1757–1768 (2011).
19. R. F. Cooper, A. M. Dubis, A. Pavaskar, J. Rha, A. Dubra, and J. Carroll, "Spatial and temporal variation of rod photoreceptor reflectance in the human retina," Biomed. Opt. Express **2**(9), 2577–2589 (2011).
20. A. Dubra, Y. Sulai, J. L. Norris, R. F. Cooper, A. M. Dubis, D. R. Williams, and J. Carroll, "Noninvasive imaging of the human rod photoreceptor mosaic using a confocal adaptive optics scanning ophthalmoscope," Biomed. Opt. Express **2**(7), 1864–1876 (2011).
21. D. Merino, J. L. Duncan, P. Tiruveedhula, and A. Roorda, "Observation of cone and rod photoreceptors in normal subjects and patients using a new generation adaptive optics scanning laser ophthalmoscope," Biomed. Opt. Express **2**(8), 2189–2201 (2011).
22. Y. Zhang, J. Rha, R. Jonnal, and D. Miller, "Adaptive optics parallel spectral domain optical coherence tomography for imaging the living retina," Opt. Express **13**(12), 4792–4811 (2005).
23. R. J. Zawadzki, S. M. Jones, S. S. Olivier, M. Zhao, B. A. Bower, J. A. Izatt, S. Choi, S. Laut, and J. S. Werner, "Adaptive-optics optical coherence tomography for high-resolution and high-speed 3D retinal in vivo imaging," Opt. Express **13**(21), 8532–8546 (2005).
24. Y. Zhang, B. Cense, J. Rha, R. S. Jonnal, W. Gao, R. J. Zawadzki, J. S. Werner, S. Jones, S. Olivier, and D. T. Miller, "High-speed volumetric imaging of cone photoreceptors with adaptive optics spectral-domain optical coherence tomography," Opt. Express **14**(10), 4380–4394 (2006).
25. R. S. Jonnal, J. Rha, Y. Zhang, B. Cense, W. Gao, and D. T. Miller, "In vivo functional imaging of human cone photoreceptors," Opt. Express **15**(24), 16141–16160 (2007).
26. R. J. Zawadzki, S. S. Choi, S. M. Jones, S. S. Oliver, and J. S. Werner, "Adaptive optics-optical coherence tomography: optimizing visualization of microscopic retinal structures in three dimensions," J. Opt. Soc. Am. A **24**(5), 1373–1383 (2007).
27. R. J. Zawadzki, B. Cense, Y. Zhang, S. S. Choi, D. T. Miller, and J. S. Werner, "Ultrahigh-resolution optical coherence tomography with monochromatic and chromatic aberration correction," Opt. Express **16**(11), 8126–8143 (2008).
28. R. J. Zawadzki, S. M. Jones, S. Pilli, S. Balderas-Mata, D. Y. Kim, S. S. Olivier, and J. S. Werner, "Integrated adaptive optics optical coherence tomography and adaptive optics scanning laser ophthalmoscope system for simultaneous cellular resolution in vivo retinal imaging," Biomed. Opt. Express **2**(6), 1674–1686 (2011).
29. E. J. Fernández, B. Hermann, B. Považay, A. Unterhuber, H. Sattmann, B. Hofer, P. K. Ahnelt, and W. Drexler, "Ultrahigh resolution optical coherence tomography and pancorrection for cellular imaging of the living human retina," Opt. Express **16**(15), 11083–11094 (2008).
30. D. T. Miller, O. P. Kocaoglu, Q. Wang, and S. Lee, "Adaptive optics and the eye (super resolution OCT)," Eye (Lond.) **25**(3), 321–330 (2011).
31. O. P. Kocaoglu, S. Lee, R. S. Jonnal, Q. Wang, A. E. Herde, J. C. Derby, W. Gao, and D. T. Miller, "Imaging cone photoreceptors in three dimensions and in time using ultrahigh resolution optical coherence tomography with adaptive optics," Biomed. Opt. Express **2**(4), 748–763 (2011).
32. J. I. W. Morgan, A. Dubra, R. Wolfe, W. H. Merigan, and D. R. Williams, "In vivo autofluorescence imaging of the human and macaque retinal pigment epithelial cell mosaic," Invest. Ophthalmol. Vis. Sci. **50**(3), 1350–1359 (2008).
33. D. Merino, C. Dainty, A. Bradu, and A. G. Podoleanu, "Adaptive optics enhanced simultaneous en-face optical coherence tomography and scanning laser ophthalmoscopy," Opt. Express **14**(8), 3345–3353 (2006).
34. M. Pircher, R. J. Zawadzki, J. W. Evans, J. S. Werner, and C. K. Hitzenberger, "Simultaneous imaging of human cone mosaic with adaptive optics enhanced scanning laser ophthalmoscopy and high-speed transversal scanning optical coherence tomography," Opt. Lett. **33**(1), 22–24 (2008).
35. M. Mujat, R. D. Ferguson, A. H. Patel, N. Iftimia, N. Lue, and D. X. Hammer, "High resolution multimodal clinical ophthalmic imaging system," Opt. Express **18**(11), 11607–11621 (2010).
36. M. Pircher, B. Baumann, E. Götzinger, H. Sattmann, and C. K. Hitzenberger, "Simultaneous SLO/OCT imaging of the human retina with axial eye motion correction," Opt. Express **15**(25), 16922–16932 (2007).
37. M. Pircher, E. Götzinger, H. Sattmann, R. A. Leitgeb, and C. K. Hitzenberger, "In vivo investigation of human cone photoreceptors with SLO/OCT in combination with 3D motion correction on a cellular level," Opt. Express **18**(13), 13935–13944 (2010).
38. R. Leitgeb, C. Hitzenberger, and A. Fercher, "Performance of fourier domain vs. time domain optical coherence tomography," Opt. Express **11**(8), 889–894 (2003).
39. F. Spöler, S. Kray, P. Grychtol, B. Hermes, J. Bornemann, M. Först, and H. Kurz, "Simultaneous dual-band ultra-high resolution optical coherence tomography," Opt. Express **15**(17), 10832–10841 (2007).

#198069 - $15.00 USD Received 23 Sep 2013; revised 1 Nov 2013; accepted 12 Nov 2013; published 25 Nov 2013

40. M. Szkulmowski, M. Wojtkowski, P. Targowski, and A. Kowalczyk, "Spectral shaping and least square iterative deconvolution in spectral OCT," in *Biomedical Optics 2004* (International Society for Optics and Photonics, 2004), pp. 424–431.
41. M. Szkulmowski, M. Wojtkowski, T. Bajraszewski, I. Gorczyńska, P. Targowski, W. Wasilewski, A. Kowalczyk, and C. Radzewicz, "Quality improvement for high resolution in vivo images by spectral domain optical coherence tomography with supercontinuum source," Opt. Commun. **246**(4-6), 569–578 (2005).
42. H. C. Hendargo, M. Zhao, N. Shepherd, and J. A. Izatt, "Synthetic wavelength based phase unwrapping in spectral domain optical coherence tomography," Opt. Express **17**(7), 5039–5051 (2009).
43. P. L. Lin, A. T. T. Shen, R. Wang, L. An, P. Li, and T. Shen, "High speed spectral domain optical coherence tomography for retinal imaging at 500,000 A-lines per second," Biomed. Opt. Express **2**, 21–31 (2011).
44. B. Potsaid, I. Gorczynska, V. J. Srinivasan, Y. Chen, J. Jiang, A. Cable, and J. G. Fujimoto, "Ultrahigh speed spectral / Fourier domain OCT ophthalmic imaging at 70,000 to 312,500 axial scans per second," Opt. Express **16**(19), 15149–15169 (2008).
45. Y. Zhang, X. Wang, and J. Wang, "High-Speed Adaptive Optics Scanning Laser Ophthalmoscope (AOSLO)," in *ARVO* (2010), p. 2311/A561.
46. Y. Zhang, X. Wang, R. Myers, J. Alexander, T. Ye, A. Roorda, and P. Gamlin, "Broad-Spectrum Adaptive Optics Scanning Laser Ophthalmoscopy," in *IOVS* (2011), p. 52:ARVO E–Abstract 5869.
47. K. Grieve, P. Tiruveedhula, Y. Zhang, and A. Roorda, "Multi-wavelength imaging with the adaptive optics scanning laser Ophthalmoscope," Opt. Express **14**(25), 12230–12242 (2006).
48. P. Bedggood, M. Daaboul, R. Ashman, G. Smith, and A. Metha, "Characteristics of the human isoplanatic patch and implications for adaptive optics retinal imaging," J. Biomed. Opt. **13**(2), 024008 (2008).
49. F. C. Delori, R. H. Webb, and D. H. Sliney; American National Standards Institute, "Maximum permissible exposures for ocular safety (ANSI 2000), with emphasis on ophthalmic devices," J. Opt. Soc. Am. A **24**(5), 1250–1265 (2007).
50. M. Wojtkowski, R. Leitgeb, A. Kowalczyk, T. Bajraszewski, and A. F. Fercher, "In vivo human retinal imaging by Fourier domain optical coherence tomography," J. Biomed. Opt. **7**(3), 457–463 (2002).
51. P. Thévenaz, U. E. Ruttimann, and M. Unser, "A pyramid approach to subpixel registration based on intensity," IEEE Trans. Image Process. **7**(1), 27–41 (1998).
52. M. D. Abramoff, P. J. Magalhães, and S. J. J. Ram, "Image processing with ImageJ," Biophotonics International **11**, 36–43 (2004).
53. S. B. Stevenson and A. Roorda, "Correcting for miniature eye movements in high resolution scanning laser ophthalmoscopy," Proc. SPIE **5688**, 145–151 (2005).
54. C. R. Vogel, D. W. Arathorn, A. Roorda, and A. Parker, "Retinal motion estimation in adaptive optics scanning laser ophthalmoscopy," Opt. Express **14**(2), 487–497 (2006).
55. R. F. Spaide, H. Koizumi, M. C. Pozzoni, and M. C. Pozonni, "Enhanced depth imaging spectral-domain optical coherence tomography," Am. J. Ophthalmol. **146**(4), 496–500 (2008).
56. C. A. Curcio, K. R. Sloan, R. E. Kalina, and A. E. Hendrickson, "Human photoreceptor topography," J. Comp. Neurol. **292**(4), 497–523 (1990).
57. M. Young, E. Lebed, Y. Jian, P. J. Mackenzie, M. F. Beg, and M. V. Sarunic, "Real-time high-speed volumetric imaging using compressive sampling optical coherence tomography," Biomed. Opt. Express **2**(9), 2690–2697 (2011).
58. R. F. Spaide and C. A. Curcio, "Anatomical correlates to the bands seen in the outer retina by optical coherence tomography: literature review and model," Retina **31**(8), 1609–1619 (2011).
59. A. Panorgias, R. J. Zawadzki, A. G. Capps, A. A. Hunter, L. S. Morse, and J. S. Werner, "Multimodal assessment of microscopic morphology and retinal function in patients with geographic atrophy," Invest. Ophthalmol. Vis. Sci. **54**(6), 4372–4384 (2013).
60. R. F. Spaide, "Questioning Optical Coherence Tomography," Ophthalmology **119**, 2203–2204 (2012).
61. W. Drexler and J. G. Fujimoto, "State-of-the-art retinal optical coherence tomography," Prog. Retin. Eye Res. **27**(1), 45–88 (2008).
62. B. Cense, N. Nassif, T. Chen, M. Pierce, S. H. Yun, B. Park, B. Bouma, G. Tearney, and J. de Boer, "Ultrahigh-resolution high-speed retinal imaging using spectral-domain optical coherence tomography," Opt. Express **12**(11), 2435–2447 (2004).

1. Introduction

The invention of scanning laser ophthalmoscopy (SLO) [1,2] and optical coherence tomography (OCT) [3] represents two major advances in ophthalmoscopy. Confocal gating [4] bestows SLO with the ability to discriminate in depth, (moderately) improved lateral resolution, and significantly enhanced imaging contrast. Theoretically, the spatial resolution of the SLO is ultimately determined by the eye's numerical aperture (NA). The lateral resolution is inversely proportional to the NA and the axial resolution is inversely proportional to the square of the NA. For an eye with perfect optical quality, when the confocal pinhole is optimized, the lateral and axial resolutions for a 6 mm pupil and 600 nm light are about 1.9 μm and 33 μm, respectively [5]. Rather than being limited by the NA of the eye, the depth resolution of OCT is dependent on the spectral bandwidth of the imaging light source being used [3]. By using broadband sources in-air axial resolutions of 1.5 μm have been reported [6,7]. However, the lateral resolution of OCT is also dependent on the NA of the eye.

In addition to the imaging mechanism, the spatial resolutions of the SLO and OCT are impaired by the optical aberrations of the human eye, especially for large pupils [5]. Consequently, the lateral resolution of both OCT and SLO is limited to about 10 μm and the axial resolution of SLO is approximately 300 μm [8–10]. To achieve diffraction-limited resolution, adaptive optics (AO) has been introduced to correct for the optical defects of the human eye [11]. AO has been integrated into both SLO and OCT to great success [8,9,12–28]. Because of the high axial and lateral resolutions, AO-OCT systems have been demonstrated to image cone photoreceptors in 3-D [29–31]. AO-SLO systems have been shown to provide resolutions that can image cone and rod photoreceptor mosaics [8,12–21]

AO-SLO and AO-OCT can be highly complementary to each other in basic science and clinic research of the retina, when used in conjunction more information of structure and processes can be revealed than when the technologies are used on their own. AO-OCT reveals the retina's cross sectional structure with unprecedented 3-D spatial resolution [30], in particular, with an axial resolution that AO-SLO cannot produce. On the other hand, AO-SLO renders better *en-face* retinal images than AO-OCT in terms of image fidelity, due to fast frame rates and the use of low coherent light sources to mitigate interference artifacts (speckle) [5,12,13,17]. Furthermore, AO-SLO can also be extended with the ability to perform fluorescence imaging [16,32], which is not possible with AO-OCT. Therefore, several groups demonstrated their pioneer work integrating both imaging modalities [28,33–35]. However, due to the technical complexity the reported systems have been compromised. Time domain OCT combined with SLO can produce images with pixel to pixel correlation in the *en-face* plane [33,34,36,37], but the OCT imaging has a slow depth scanning speed and reduced sensitivity compared to Fourier domain (FD) OCT systems [38]. Using separate scanners to guide the SLO and OCT imaging beams allows FD-OCT to be performed simultaneously with high speed SLO [28], but requires differing paths guiding the light to the eye. This means that the AO can only optimize the imaging of one of the modes. Imaging simultaneously also limits the amount of light that can be used in each mode. Alternatively, imaging can be performed sequentially which allows the same imaging path to be used by the SLO and OCT [35], but the demonstrated system used swept source OCT with a central wavelength of 1070 nm. Using such a source does increase depth penetration compared to systems using light with a central wavelength around 850 nm, but axial and lateral resolution are both reduced due to the longer wavelength. The goal of this manuscript is to present our dual-modal AO-SLO-OCT by extending an existing AO-SLO system with a free space FD-OCT.

The ideal spectral shape for a light source used in OCT should produce no sidelobes in the axial point spread function (PSF), e.g., a Gaussian shape. However, it is often the case that a source may provide a broad spectrum but with a non-ideal spectral shape. One option is to use optical shaping methods to convert a source's spectrum from a non-ideal spectral shape into an ideal one, such as Gaussian [39]. These methods can be costly and may significantly reduce the available power of the source [7]. Digital shaping methods such as those using deconvolution [40,41] can optimize the coherence profile, but these involve complex algorithms that require a great deal of computing time. Simpler shaping methods are also available such as passing the detected spectrum through a window [42,43], which may only reduce sidelobes, rather than eliminating them, or using a function to modify its shape [44], which can be plagued by increased noise in the image. We present a combination of the windowing and function digital spectral shaping techniques that requires little computing time, reduces sidelobes and minimizes image degradation to noise and loss of resolution.

2. System description and methods

2.1 The AO-SLO

The AO-SLO is an upgraded system of an earlier generation MEMS-based AO-SLO [12]. It has previously been reported at conferences [45,46].

The light source of the AO-SLO is a superluminescent diode (SLD) (Broadlighter S840-HP, Superlum, Russia), it's wavelength centered at 840 nm with a bandwidth of 50 nm (FWHM). The light is collimated after its single mode output fiber and then is fed into the system by a beam splitter (BS) with 10/90 reflection/transmission ratio, as shown in Fig. 1. 10% of the light is reflected to the sample arm consisting of a series of relay telescopes (S1-S8), the horizontal scanner (HS) (8 KHz CRS, General Scanning, Billerica, MA), the vertical scanner (VS) (6200H, Cambridge Technology, Inc., Bedford, MA), and the deformable mirror (DM) (Hi-Speed DM97-15, ALPAO SAS, France), and is guided to the eye. The pupil size of the AO-SLO was set at 6 mm in diameter. Light reflected or backscattered from the retina follows the inverse path back to the 10/90 beamsplitter where 90% of the light transmits to the detection channel. 8% of the light is picked up by a pellicle beamsplitter to the wavefront sensor (WFS). The rest of light goes to the detectors (H7422-50, Hamamatsu, Japan). The light is converted to an electronic signal, further conditioned to a pseudo-video format [13], and acquired by the computer forming the AO-SLO videos.

The WFS is a custom high speed device based upon a CMOS camera (MicroVista®-NIR, Intevac Inc., USA) whose spectral response is optimized for near infrared light. The wavefront sensor is able to measure the wavefront at a frame rate of 100 Hz, providing the feedback control information in the AO system for real time compensation of the wavefront aberration. A lenslet array of 0.3 mm x 0.3 mm pitch and 7.6 mm focal length (0300-7.6-S, Adaptive Optics Associates, Cambridge, MA) samples the wavefront in 193 sub-apertures with the 512 x512 pixel sensor. From the camera's signal an in-house written program computes the required shape of the DM to make a correction. The DM is driven by 97 actuators with maximum stroke of 60 μm. The updating frequency of the AO loop can be as high as 100 Hz in the human eye, compared to most reported AO systems for retinal imaging that run with a rate about 30 Hz.

2.2 Extension to AO-OCT and dual modal imaging

To achieve AO-OCT imaging, the system was adapted by adding a reference arm and a spectrometer. Also shown in Fig. 1, light that is transmitted through a 10/90 beamsplitter (BS) from the source is back reflected and a portion enters the detection arm. The reference arm is path length matched to the sample arm. An optical trombone provides adjustment of the reference arm length and a water filled cuvette is placed in the path to compensate for dispersion in the eye.

The light from the reference beam and the sample beam form the interference signal for the OCT imaging. Before the AO-SLO photo-detector, a flip mirror (FM) directs the lights to the OCT channel consisting of a relay telescope and a spectrometer. A pinhole is placed at a point conjugate to the retina in the telescope. Light is collimated after the pinhole and is dispersed with a 1800 lines/mm transmissive diffraction grating and then focused onto a line scan camera (spL2048-140km, Basler, Germany) working with the vertical pixels binned. With the light source being used here the spectrum covers 1400 of the 2048 pixels.

Because the resonant scanner of the AO-SLO is too fast for OCT imaging, only the slower vertical galvo-scanner is used in OCT mode. This means that it is not possible to collect volume images with the OCT, but only B-scans in the vertical direction at the present time. When imaging in the OCT mode, the galvo-scanner is controlled by a signal generator, which also triggers the frame grabber (NI-PCIe-1433, National instruments, US) to synchronize the image acquisition with the scan. For each frame, 512 lines are collected. Images can be acquired at a frame rate up to 140 Hz. Often slower rates were used so the signal to noise ratio

(SNR) can be increased, especially when imaging older patients who are more likely to have opaque ocular media that reduces the amount of light returned, such as cataracts.

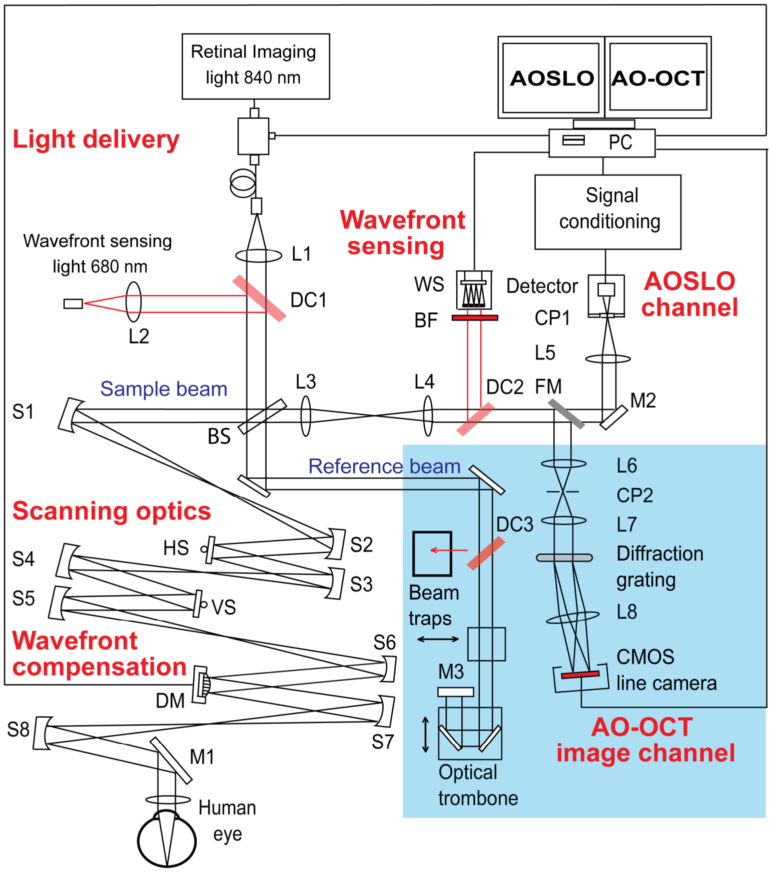

Fig. 1. A schematic diagram of the presented system. The parts highlighted in blue were added to the system to facilitate OCT imaging. L1-8; lenses, S1-8 Spherical mirrors, DC1-3; dichroic mirrors, BS; beamsplitter, HS; Horizontal scanner, VS; vertical scanner, DM; deformable mirror, BF; bandpass filter, WS; wavefront sensor, CP1 and 2; confocal pinholes, FM; flip mirror, M1-3; plane mirrors.

To avoid the unwanted light from the reference arm intruding into the wavefront sensor, a diode laser with wavelength of 680 nm is added for wavefront detection for both AO-SLO and AO-OCT modes. The light is fed into the system by a dichroic mirror (DC1). It is collinear with the imaging light through the scanning optics and reaches the retina and the reflected light follows the ingoing path back to the 10/90 beamsplitter (BS) and enters the detection channel where the pellicle beamsplitter is replaced by a second dichroic mirror (DC2), which reflects 95% of the light to the wavefront sensor. To further prevent any residual 840 nm light reaching the sensor, a bandpass filter is also placed in front of the wavefront sensor. To prevent 680 nm light entering the WFS from the reference arm, a dichroic mirror (DC3) reflects this light into a beam trap.

Using a beacon light for wavefront sensing has been previously reported [47,48]. Chromatic aberration in the human eye can cause the beacon and imaging light to focus at different points, axially and transversally. The AO-SLO was initially optimized for imaging with the 840 nm SLD light, so that the pinhole is conjugate to the source position. When the beacon light (680 nm) was implemented into the system, the SLD was turned off and the original pellicle beam splitter for the wavefront sensor was kept in place. The beacon light was first set to a power of 30 μW and its position was adjusted to so that a retinal image showing clear cone mosaic with the AO-SLO pinhole and photodetector positions unchanged. Then we replaced the pellicle with the dichroic mirror DC2. This is a process has been discussed by Grieve *et al* [47] It is important to align the beacon light focus on the same plane that the imaging light does, i.e., minimize the longitudinal chromatic aberration, so that the AO-SLO can produce clear photoreceptor mosaic when AO loop is closed. While the transverse chromatic aberration may cause focus of the beacon light to be displaced from the focus of the imaging, however, the transverse shift between the two beams in the human eye may be within a range of 1-2 arcminutes [47], which is much smaller than the isoplanatic zone of the human eye [48] and AO can compensate the aberration. The beacon light power was set at 15 μW for wavefront sensing.

To minimize the introduction of additional aberration, dichroic mirrors with high surface flatness were selected. The residual aberration introduced by the dichroic was measured using a model eye by comparing the wavefronts recorded switching DC2 with the pellicle beamsplitter. The wavefront aberration introduced by the dichroic mirror with a beam diameter at the WFS of 4.5 mm beam was smaller than 0.02 μm (RMS).

The two imaging modes are switched by the flip mirror (FM). In the AO-SLO mode, the flip mirror is open (allowing the light to be collected by the AO-SLO detector), and a beam trap is used to completely absorb the light from the reference arm. In AO-OCT mode, the flip mirror is closed (allowing the light to be reflected towards the AO-OCT spectrometer), and the beam trap is removed allowing the light from the reference arm to enter the detection channel.

2.3 Imaging protocol

The study followed the tenets of the Declaration of Helsinki and was approved by the Institutional Review Board for Human Use (IRB) at the University of Alabama at Birmingham. Written informed consent was obtained after the nature and possible consequences of the study were explained. Before imaging, the pupil of the subject was dilated with 1.0% tropicamide and 2.5% phenylephrine hydrochloride. The subject’s head was aligned and stabilized with the use of a head mount with a chinrest. A fixation target consisting of a blue light dot moving on a calibrated grid was placed in front of the eye via a pellicle beam splitter to help the subject’s fixation. The power incident on the cornea is 0.5 mW, well below the maximum permissible exposure level of the ANSI standards [49]. An SLO scan of the macula (20° field of view, made of a montage of 1° field of view, 512 line AO-SLO images) was first taken and the positions of areas of interest were marked for the AO-OCT investigation. During the AO-SLO scan the beam on the same part of the retina is less than 10 s. The AO-OCT B-scans were acquired across a field of view of 1° or 2° for less than 60 s. Prior to OCT imaging, SLO images were acquired at the marked positions to ensure that the OCT images could be correctly placed in a larger image. Images and measurements from 5 subjects are used in this paper.

2.4 Image processing

The first step in the AO-OCT processing is to resample the data in each line so that it is linear in k-space [50]. Next, in order to obtain a Gaussian coherence profile the spectrum is reshaped using a novel technique that will be presented next. The DC spectrum is then removed from each line leaving only the fringes [49]. This significantly reduces the DC (or zero Hertz) term from the Fourier transform and removes any fixed pattern noise. The lines may also be zero padded to increase the sampling density of the result in the Fourier transform.

AO-OCT image sets were registered using the StackReg plugin [51] for ImageJ [52] and when a stable group was found, averaged to produce a single image with reduced noise. The

#198069 - $15.00 USD Received 23 Sep 2013; revised 1 Nov 2013; accepted 12 Nov 2013; published 25 Nov 2013

number of images used for averaging is dependent on a subject's eye motion and the frame rate being used, but typically sets of 7 suitable frames could be found and averaged when imaging at a frame rate of 100 Hz.

For the AO-SLO, image distortion caused by nonlinear scanning of the resonant scanner and by eye movements was eliminated by customized software [53,54]. Registered images were averaged to enhance signal-to-noise ratio. Then images taken at different retinal locations were aligned with Photoshop (Adobe Systems Inc., Mountain View, CA) to create a continuous montage.

2.5 Spectral shaping

In the presented system the SLD being used has a non-ideal spectral shape. We propose a digital spectral shaping method that combines two existing methods to rectify this. The first method, referred to as the window method, passes the camera's response through a Gaussian window [42,43]. The second technique, referred to as the function method, reshapes the spectrum to a Gaussian, rather than just filtering it [44]. Our method first uses the function method to reshape the non-ideal source and then the window method is applied and will be referred to as the combined method.

The window method in effect acts as a low pass filter. After Fourier transform the resulting coherence profile may have reduced but not eliminated sidelobes. The function method provides a coherence profile that is of a near perfect Gaussian shape, but at the cost of a decreased SNR. This decrease in sensitivity can be explained by the difference between the process of the window and function methods. At the extremities of the raw spectrum the signal mostly consists of noise, as the light levels here are low. When the shaping methods are applied, the window method tends to suppress the edges of the spectrum and the function method tends to amplify them. Because the interference fringes here are weak, there is only a small change to the signal in both cases, but the function method sees a significant increase in noise, while the window method causes a decrease. By combing the two techniques, the function method yields an ideally shaped spectrum and then the window method suppresses the increased noise at the edges of the spectrum.

In this paper we test the window, function and combined methods of spectral shaping and compare them to the unshaped spectrum. For the window method a Gaussian with a FWHM width of 798 pixels and amplitude of 1 was used. The value of each pixel in the raw spectrum is multiplied by the corresponding value of the window. The integral of the shaped spectrum is then set to the integral of the raw spectrum by a multiplication.

The function method is performed by measuring the detected spectrum by averaging the camera response for all lines acquired for an image, negating the fringes due to their random phases. A function is then calculated by dividing this by a Gaussian function with a FWHM width of 798 pixels whose integral is equal to the integral of the spectrum. The Gaussian function is also modified by setting the magnitude at the beginning and ends to zero, preventing high frequency artifacts that obscure the image when the Gaussian function's width is large. The generated function is then used to divide each image line before Fourier transform.

The combined method first utilizes the function method in the same manner, then is windowed by a second Gaussian function. As both stages of the combined method shape the spectrum, a wider Gaussian function is used for the function step than when only the function method is used. Here a FWHM of 1582 pixels was used. The width of the windowing Gaussian was 798 pixels.

When choosing the widths of the Gaussian functions, the values were determined by monitoring the FWHM of the coherence profile; the widths were chosen so that the resolutions obtained by the shaped spectra were equal to that of the unshaped spectrum. In all cases the normalization of the integrals maintains the signal magnitude of the raw spectrum in the shaped spectra.

#198069 - $15.00 USD Received 23 Sep 2013; revised 1 Nov 2013; accepted 12 Nov 2013; published 25 Nov 2013

3. Results

3.1 Spectral Shaping

The spectrum of the uncorrected light source and the spectra generated using the window, function and combined methods are shown in Fig. 2(a). All spectra were obtained after resampling for linear *k*-space. Figure 2(b) shows the coherence functions of the raw spectrum and the shaped spectra using the three methods. The profiles were obtained by averaging 512 A-scans of a single scattering sample placed at in the focus of a model eye. The scans were zero padded before the Fourier transform to increase the number of plot points.

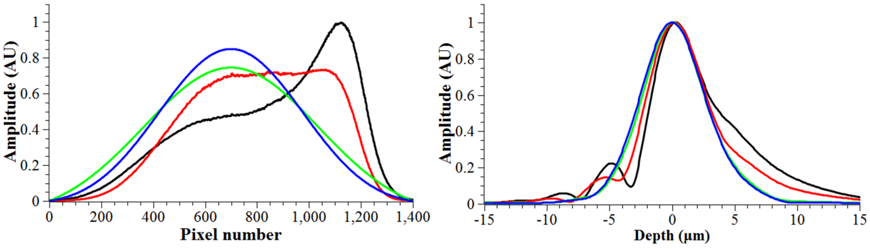

(a) **(b)**

Fig. 2. (a). Spectra obtained from averaging all 512 lines used to generate an image. Figure 2(b) Normalized coherence profiles from an average of 512 A-scans. For both graphs; black- raw spectrum, red- window method, green- function method, blue- combined method. In this case, the coherence profiles of the function and combined methods are almost identical and very close to an ideal Gaussian shape.

It can be seen that spectral shaping using the window method results in a coherence profile that still contains sidelobes, although reduced. The function and combined methods both result in a profile that is of a near perfect Gaussian shape. All widths are approximately equal, as was intended by the design of each method. Measurements of the FWHM and e^{-2} width of each coherence profile are shown in Table 1, which also includes SNR measurements, defined as the ratio of the square of the peak signal and the square of the noise [38]. The e^{-2} width is significantly influenced by the presence of side lobes or a skewed coherence profile. The noise is taken as the average standard deviation of 512 A-scans with no sample light present and the DC spectrum subtracted. The signal magnitudes were taken from the coherence profiles displayed, but before normalization.

Table 1. The FWHM, e^{-2} width and relative SNR of the three methods

Method	FWHM (µm)	**e^{-2} width (µm)**	SNR (dB)
Raw	5.7	16.1	0
Windowed	5.6	13.9	0.3
Function	5.7	10.9	−2.0
Combined	5.8	10.9	−1.0

The spectral shaping helps reveal fine structures and removes artifacts from images. An example is given in Fig. 3, which shows the same retinal image processed with and without spectral shaping. The combined method was used. Evidently, the spectral shaping increases the clarity and the fidelity of the images. In particular, the stratified layers of the retina become more distinct, as shown in the images; for example, at the inner segments, indicted by (a), the layer between the outer segment tips (OST) and retinal pigment epithelium (RPE) indicated by (b), and the interface between the RPE and choriocapillaris, (c). The inner layers are also sharper, e.g., the capillaries indicated by the red arrows.

#198069 - $15.00 USD Received 23 Sep 2013; revised 1 Nov 2013; accepted 12 Nov 2013; published 25 Nov 2013

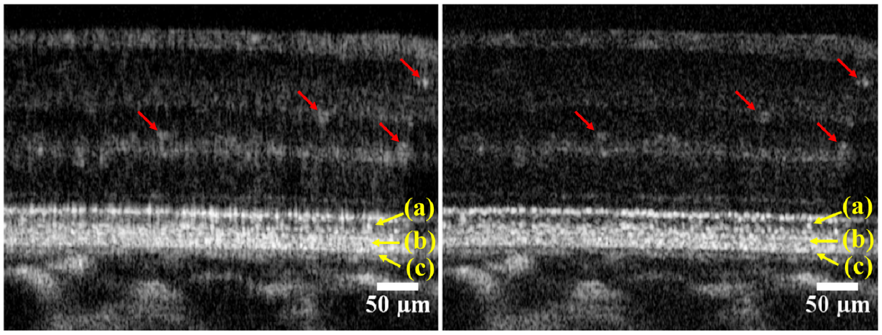

Fig. 3. Retinal images taken a 4° nasal to the fovea center from a subject (#1) in good retinal health. The images are from the same B-scans and have been processed identically, but the image on the right was spectrally shaped and the image on the left was not. The red and yellow arrows point to features discussed in the main text. The images are in logarithmic grey scale. These images were taken with the outer retina closest to zero optical path difference, minimizing the sensitivity loss to the choroid and inner retina due to roll-off [55]. The images were taken at a frame rate of 50 Hz and are average of 5 frames.

3.2 Adaptive optics performance

The AO can reduce the root-mean-square (RMS) wave aberration to less than 0.05 µm in most eyes. Figure 4 shows retinal images taken with the AO switched on and off. Clearly, with the AO on the image is much brighter and sharper. In these images the focus was set to the inner retina which highlights the layers here and provides a balance between the brightness of the photoreceptor-RPE complex and retinal nerve fiber layer (RNFL). Comparing the average brightness of the images in this region shows an increase in the signal of 8.0 dB. Using images with the focus set to the photoreceptor-RPE complex, the average increase in the OCT peak signal with AO compensation is 8.2 dB. This was measured by comparing images from the same position in a healthy eye and averaging the peak signal from the RPE across all 512 lines. When a similar measurement was performed using a model eye consisting of a lens and a diffuse reflector, the improvement was found to be 8.7 dB. The OCT sensitivity, as measured from a surface of a glass slide positioned close to zero OPD at a camera line rate of 50 kHz is 91 dB with the AO compensation.

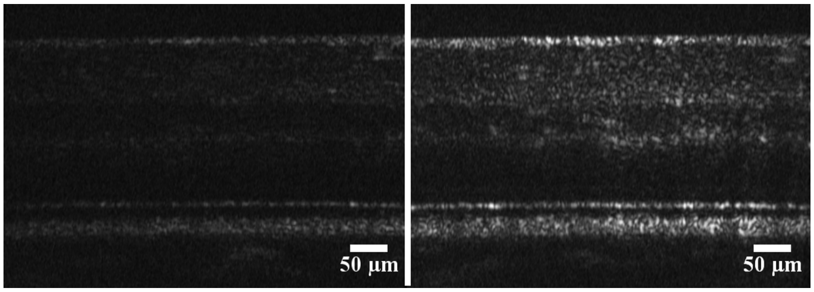

Fig. 4. Examples of AO-OCT retinal images with the adaptive optics switched off (left) and on (right). The image was taken at 4° temporal eccentricity to the fovea centre in subject (#2) who is in good retinal health. The frame rate is 100 Hz, and 5 frames are averaged in both images. The images have a linear grey scale.

3.3 AO-SLO-OCT imaging of healthy retinas

Figure 5 shows an AO-OCT image acquired from a healthy eye, approximately 2° nasal from the fovea center with the focus on the photoreceptors. The figure shows similar structures to those presented in the literature [27,30,31]. The AO correction for ocular aberration provides an improvement such that the lateral resolution of the OCT sufficient to resolve the IS/OS and

#198069 - $15.00 USD Received 23 Sep 2013; revised 1 Nov 2013; accepted 12 Nov 2013; published 25 Nov 2013

OST of individual photoreceptors. Meanwhile, the depth of focus is reduced, so the inner layers of the retina appear dim as the focus was placed around the photoreceptor-RPE complex. By using a log scale, the inner retinal structure may become clearer, but this reduces the apparent resolution; a FWHM is increased by approximately 80% by logarithmic scaling which may obscure details such as the photoreceptors.

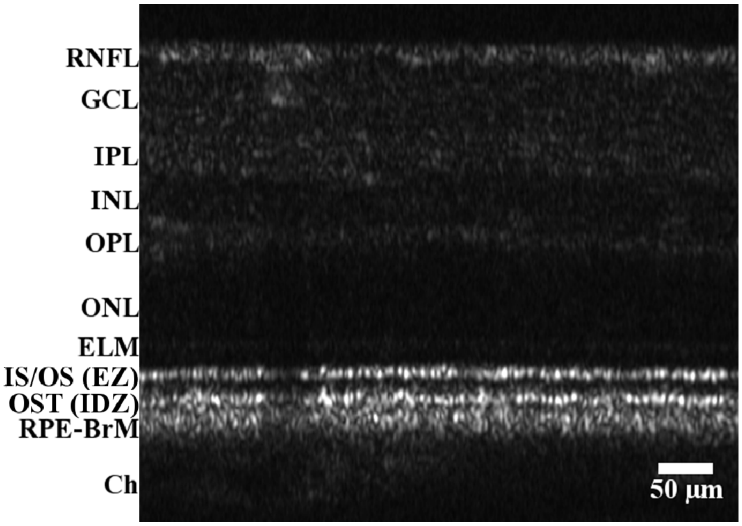

Fig. 5. AO-OCT B-scan of a healthy retina (subject #3). 2° nasal from the central fovea with the focus at the photoreceptors. The image is displayed with a linear grey scale. The frame rate was 50 Hz and this is an average of 7 images. The scale, indicated by the bar has a 1:1 vertical/horizontal ratio and has been corrected for the refractive index of retinal tissue (assumed to be n = 1.33). The marked layers are RNFL; retinal nerve fiber layer, GCL; ganglion cell layer, IPL; inner plexiform layer, INL; inner nuclear layer, OPL; outer plexiform layer, ONL; outer nuclear layer, ELM; external limiting membrane, IS/OS: inner segment/outer segment junction; EZ: ellipsoid zone; OST; outer segment tips, RPE-BrM; retinal pigment epithelium/Bruch's membrane complex, Ch; Choroid. The IS/OS and the OST are also claimed as the EZ (ellipsoidal zone) and the IDZ (interdigitation zone), respectively.

Figure 6 is a montage of AO-SLO images showing clearly resolved photoreceptors around the fovea and out to a wider eccentricity. Thumbnails taken from the wide field image show selected areas with more detail. OCT scans at these positions were also taken and are shown. It is evident that high lateral resolutions were achieved in both imaging modalities. Axially, the OCT images show clearly resolved layers and IS/OS of the photoreceptors at all positions.

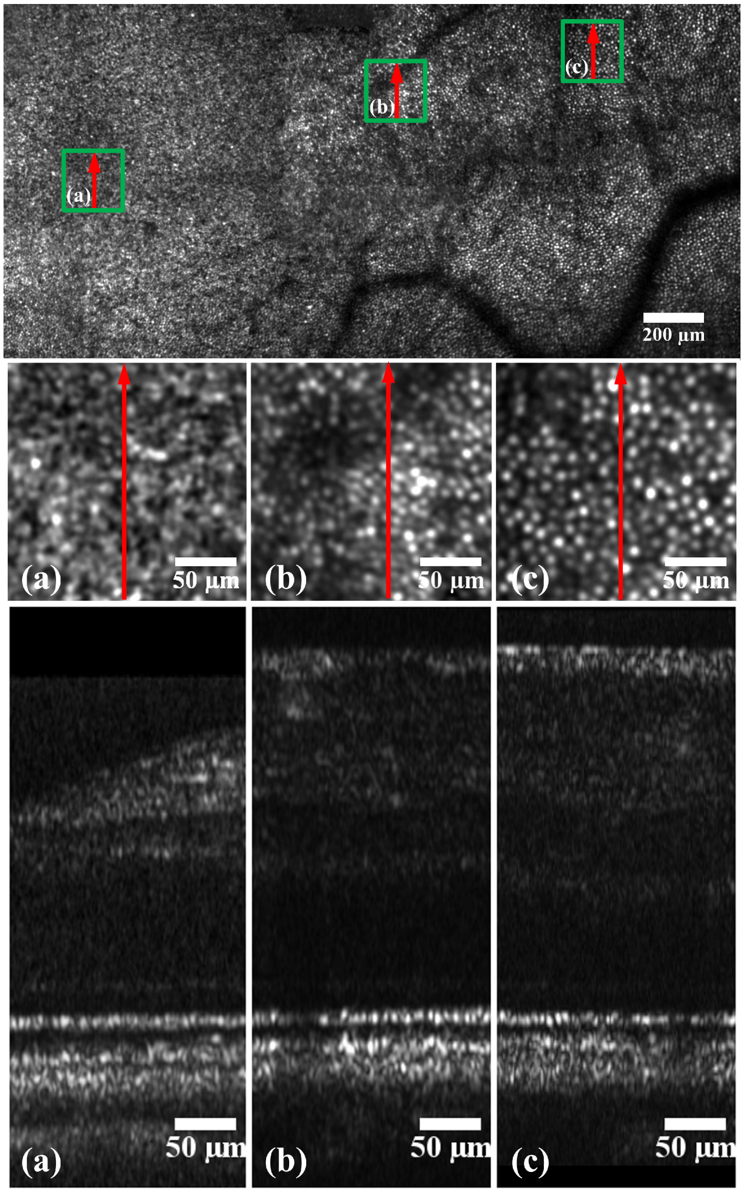

Fig. 6. AO-SLO thumbnails (middle) taken from an AO-SLO montage (top) and AO-OCT (bottom) images taken at different retinal eccentricities from subject #3 in good retinal health. The bright spots in the AO-SLO images are cone photoreceptors. Each AO-SLO image is a registered set of 20 AO-corrected images. All images have been corrected for distortions due to eye movements and the nonlinear scan [54]. The arrows on the AO-SLO images indicate the position and direction of the OCT scan, the arrow direction corresponds to right to left in the OCT images. The green squares on the SLO montage show where the enlarged SLO images are located.

3.3 Measure of the photoreceptor spacing

The cone photoreceptor spacing was measured from the images in Fig. 6 by counting the number of resolvable cells across a 50 µm line drawn in the IS/OS. Dividing the count by the distance gives an estimate of the center to center spacing. The results are shown in Table 2. This measurement is sensitive to distance from the retina to the nodal points of the eye's lens system, as this length is used to convert the scanning angle to scan length. Here this length was assumed to be 16.9 mm, from the Gullstrand eye model, but there is variability from person to person [56] that may be affecting the accuracy. Even so, a similar measurement from the AO-SLO images confirms the AO-OCT measurement and these measurements are consistent with reported measurements in the literature [22,25,57].

Table 2. Measurement of the cone spacing from OCT images

Location (degrees from fovea)	Spacing (μm)
1°	4.5
2°	5.6
3°	6.3

3.4 Measure of the IS/OS length and axial positions of individual photoreceptors

Currently the outer retinal structures seen in OCT images are in debate, in particular the layer traditionally labeled as the IS/OS [58–60]. It has been argued that this layer may correspond to backscattering from the ellipsoidal mitochondria in the inner segment of photoreceptors, leading to the suggestion it should be named as the ellipsoidal zone (EZ) [58,60]. If this were true, this layer should have a thickness of between 14 and 16 μm [58]. We measured the FWHM of the IS/OS by averaging that measured from 25 individual photoreceptors between 2° and 3° nasal from the foveal center in 4 subjects. The results are listed in Table 3. Measurements at other eccentricities away from the fovea (between 3° and 10° eccentricity) were performed in one subject, at each point a similar IS/OS length was found. To check for the effects of dispersion, the thickness of the foveal reflex (the hyper-reflective band seen directly over the center of the fovea) was measured from the same eye and was found to be 4.7 ± 0.13 μm from 5 measurements.

Table 3. Measurement of the IS/OS (EZ) thickness

Subject number	IS/OS (EZ) thickness (μm)	Standard deviation
1	6.0	0.5
2	5.9	0.5
3	6.2	0.6
4	6.1	0.5

It can be seen from Fig. 5 that the depth position of the IS/OS varies between individual photoreceptors. To assess this variation, a single, unsaturated, and well resolved image, which was taken at 2° eccentricity to the fovea center was selected. The image was one of the contributing frames to the image of Fig. 5. The depth positions of the reflection corresponding to the IS/OS of 16 adjacent photoreceptors were measured. A short distance was used to minimize the effects of axial eye motion, if any was present. The depth was measured by the IS/OS peak relative to zero OPD. It was found that the standard deviation of the depth of the IS/OS was 1.3 μm, with a maximum-minimum deviation of 5 μm (both measurements corrected for the refractive index of retinal tissue).

3.5 Imaging of drusen in a patient with age-related macular degeneration

Figure 7 shows images from a patient diagnosed with age-related macular degeneration (AMD). This disease is characterized by lesions known as drusen that are pathological extracellular materials accumulating between the Bruch's membrane and the RPE, deforming the RPE and photoreceptor layers. Drusen have a variety of appearances in OCT images which may be classified [46]. Figure 7 shows an AO-SLO image with corresponding AO-OCT images of a large soft druse at the fovea. The subject was a 78 year-old man (white non-Hispanic) with non-neovascular AMD at intermediate stage (The Age-Related Eye Disease Study (AREDS) grade 6, best corrected visual acuity (BCVA) 20/30).

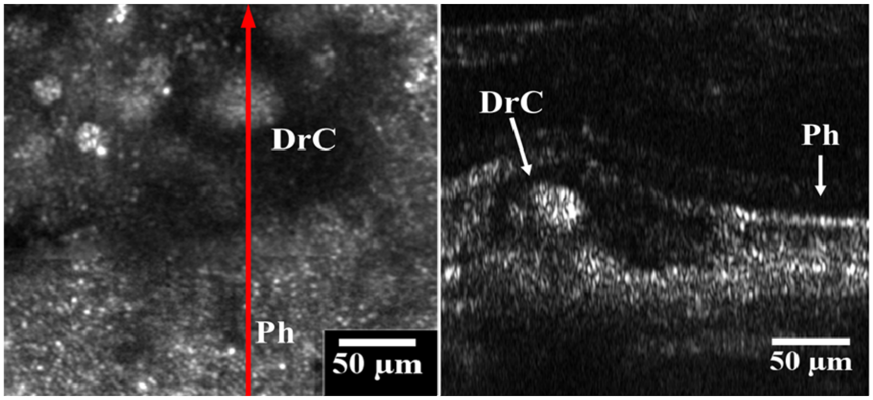

Fig. 7. Images of a large druse at the fovea. Left panel is the AO-SLO image, showing the retina overlying the drusen with significantly reduced reflectivity. Outside the dark area, the contiguous reflective spots are cone photoreceptors (Ph). The red arrow marks where the AO-OCT B scan was taken. The arrow direction shows the right to left direction of the AO-OCT image (right panel). The AO-OCT image has a 1° field of view. The label Ph shows preserved photoreceptors and the label DrC shows the core of the druse in both the SLO and OCT images.

The lesion can be seen to deform the overlying photoreceptor layers in the OCT image. The enhanced resolution given by the AO correction allows photoreceptors to be resolved to the right of the drusen in the IS/OS (marked Ph). Above the druse the IS/OS band becomes less distinct. Reflectivity is also reduced in the OST around the druse. This corresponds to the hypo-reflective region surrounding the druse core (marked DrC) in the AO-SLO image. It is interesting to note the granules in the hyper-reflective core of the druse in the AO-OCT image. They are close in axial length to the resolution of the system, so it is not known whether these granules are real lesion particles or just speckle artifacts. However, the granular nature of the druse is seen in the AO-SLO image, which should have significantly reduced speckle because image averaging and the use of a broadband source. This suggests that some of the features seen in the druse core are real, but higher axial resolution imaging utilizing a broader source may help examine if the features are speckle artifact or not.

4. Discussion

The AO-OCT was implemented with a free space Michelson interferometer scheme in an existing AO-SLO system, requiring a minimum of optical components and avoiding light loss that can occur in an optical fiber based system. The pinhole size at the spectrometer can be changed very easily, allowing for a better balance between lateral resolution and the amount of light for imaging. This is more difficult for systems that use fiber optics to guide light to detectors. The system uses the same light source for the AO-SLO and AO-OCT imaging. More importantly, because the AO-SLO and AO-OCT imaging share the same light source and path through the sample and detector arms the correction provided by the AO is optimal in both modes. Thus, both the two imaging modalities achieve equal performance.

While the system avoided compromises made by other systems presented in the literature, it was compromised in some ways. As described in section 2.2, the OCT may only be scanned in one direction, so volumetric imaging is not possible, but this could be mitigated by adding another galvo-scanner to the sample arm and still retaining the common path.

The spectral shaping method presented here produces a reshaped spectrum that is very close to a Gaussian shape. It has a great improvement over the window method, in terms of sidelobe reduction, as indicated by the reduced e^{-2} width. Compared to the function method, it has been demonstrated to have improved noise suppression, though the improvement is not significant with this light source. It would seem reasonable that the magnitude of these improvements is dependent on the original source shape. The source used in this system, although non-ideal, is not as misshaped as many broader sources that are available where spectral shaping becomes more important. For example, Potsaid *et al* [44] applied the function method on a source with broader spectrum and having multiple peaks and troughs in its profile. They reported a decrease of resolution of 0.5 μm, which was not observed in our study. We expect, even with such a source, the combined technique should still shape the spectrum with less noise introduced than with the function technique alone. Thus, it would be prudent to test the method with a broader source to see if that can be reshaped using this technique without increasing the noise or lowering resolution. The signal processing does not significantly increase the computation time, as it only adds a simple multiplication to the routine.

We do not claim that the extension of a SD-OCT module in an existing AO-SLO system presented in this paper represents the best combination of the two imaging modalities for every application. But it is important to note that cellular level imaging can be achieved in both *en face* and cross sectional planes with a single instrument using the same light source and scanning optics. This is critical in answering important questions in basic and clinical research of the retina. As exampled in this paper, the AO-SLO acquires high quality images of the cone mosaic, while the AO-OCT reveals the depth information of the reflecting layers of individual cells with equal lateral resolution. The AO-SLO-OCT images helped understand how the photoreceptors were affected by an underlying druse. In the case presented in this paper, the photoreceptors overlying the drusen core imaged by the AO-SLO shows a similar reflectivity to that of the preserved photoreceptors outside of the affected area. But from the AO-OCT image, we can see that the photoreceptors are significantly deviated from the normal position in the retina and the outer segments tips are indistinct, indicating a significant degeneration.

It is possible the smallest photoreceptors seen in the OCT images, are an artifact due to speckle, e.g. those seen in Fig. 6(a) and Fig. 7. However the accompanying AO-SLO images show clearly resolved contiguous mosaic of cones. The AO-SLO imaging is largely speckle free due to the averaging of multiple frames and the use of a broadband source reducing interference artifacts. While there is ambiguity when viewing solely the AO-OCT images, when used in conjunction with the AO-SLO the conclusion that photoreceptors are imaged by the AO-OCT can be made with more confidence.

The second hyper-reflective photoreceptor band has been traditionally considered as a single surface interface [59] and labeled as the IS/OS junction (for example, see Drexler and Fujimoto [61] or Zawadzki *et al* [27]). The recent claim that this band was formed by the light scattered from the EZ, would suggest that the band's thickness would be greater than a single interface reflection. It should be noted that this deduction [58] was based upon the measurement of the thickness of this band in OCT images acquired using a conventional instrument. Thus, the measurement could be affected by the low lateral resolution of the system used. From the AO-OCT images presented here we can see that there is some variance in the depth position of the IS/OS between individual cells. A system with low lateral resolution would measure multiple IS/OS peaks in each A-scan. The variance may lead to the appearance of a thicker band than is true, as the OCT signal is the sum of all the reflectors that the beam is incident on and the beam from a low resolution system would cover a bundle of cells. Our measurement shows that the maximum-minimum position deviation can be up to 5 μm. At this position, a laterally low resolution system would measure a significantly thicker layer than the AO enhanced system; thus it may lead to or influence incorrect interpretations to the origins of this band.

Our measurement from individual photoreceptors shows that the thickness (6 μm) of the IS/OS reflection is significantly shorter than the length of the ellipsoidal zone (14 to 16 μm). On the other hand, our measured thickness is longer than the expected axial resolution (4.3 μm). To exclude the possibility of dispersion induced broadening, we measured the FWHM of the foveal reflex, which has been considered as a single surface reflector suitable for *in-vivo* measurement of the axial resolution [62]. The result is 4.8 µm, narrower than that of the IS/OS band. This suggests that the measurement of the IS/OS thickness was only minimally affected by dispersion and other broadening effects such as water absorption being spectrally unequal. If both layers were single surface reflections, equal thicknesses would be expected. Thus, our measurements imply that the IS/OS is not from a single interface reflection and it does not originate from the whole ellipsoidal zone of the photoreceptors either. Further investigation of the IS/OS band with higher axial resolution given by a broader source with accurate dispersion compensation and careful compensation of chromatic aberration's impact on lateral resolution [27,29] is warranted.

5. Conclusion

A dual-modal, free space AO-SLO-OCT system has been presented. To enhance the visibility of features in the AO-OCT images a combined digital spectral shaping method was developed. This reduces the sidelobes produced in the coherence profile when a non-Gaussian light source is used whilst minimizing any increase in noise. The system was used to obtain *in-vivo* images from healthy and diseased retinas. An integrated AO-SLO-OCT that can produce the same imaging quality in both modes and acquire AO-SLO and AO-OCT images with accurate cell-to-cell registration remains an important direction.

Acknowledgments

This project was supported by funding from EyeSight Foundation of Alabama, International Retina Research Foundation, Songs for Sight, Buck Trust of Alabama, NIH 1R21EY021903, NIH P30 EY003039, Research to Prevent Blindness. The authors gratefully thank Christine A Curcio PhD for advising on labeling of the retinal layers, and thank Xiaolin Wang MS for assistance of image acquisition and AO-SLO image processing.